Sea-bed scattering and reflection contributions to the short-range acoustic impulse response: measurements and modelling

Sven IVANSSON, Per-Axel KARLSSON

Swedish Defence Research Agency
FOI Kista, SE-16490 Stockholm, Sweden
sven.ivansson@foi.se, per-axel.karlsson@foi.se

A short-range experiment in shallow water has been performed to assess the various contributions to the impulse response. A sound source emitted pulses, centered at 25 kHz, that were registered by an array some 50 m away. The impulse response recordings show initial isolated peaks, followed by long decaying spiky tails. A 3-D ray model, Rev3D, was used to model the measured time traces. The initial peaks were identified as direct and multi-path propagation arrivals, while the decaying tails arise from bistatic reverberation involving the bottom and the sea surface in an elliptical area, with the source and receiver positions as focal points. Beam-forming with the receiver array was applied to locate the parts of the bottom with the most significant contributions to the impulse response, and to suggest an improved reflection-coefficient as well as scattering-kernel values. Rev3D modelling with energy-density maps for selected time intervals, and time traces for energy-weighted averages of various parameters, such as the arrival angles at the array, was also applied for this purpose.

Keywords: ray-tracing, bistatic reverberation, beam-forming

1. Introduction

Sound propagation modelling, with modelling of the channel impulse response as an essential ingredient, is important for sonar performance prediction and evaluation of signal processing algorithms. However, sea-bed and sea-surface scattering, as well as multi-path arrivals, make the impulse response complicated [1]. Traditional 2-D propagation modelling is not always sufficient, e.g., [2]. A large variety of channels must be handled for model-based simulators of underwater communication and sonar performance [3]. The sea-surface and bottom scattering affect the signal coherence, and failure to model the scattering contributions correctly may lead to erroneous estimates of target detection ranges.

The present paper reports results from a short-range experiment in shallow water, under well-controlled conditions, designed to assess the various contributions to the impulse

response. The measurements were made at the beginning of October, with a downward refracting sound-speed profile below the depth 20 m. A sound source mounted at depths between 5 and 25 m emitted FM and short CW pulses, centered at 25 kHz, that were registered by an array at depth 7.5 m some 50 m away. The water depth at the source and receiver location was 29 and 16 m, respectively. Geologically, see Fig. 1, there is a transition of bottom type from glacial clay at the source, to crystalline rock at the receiver.
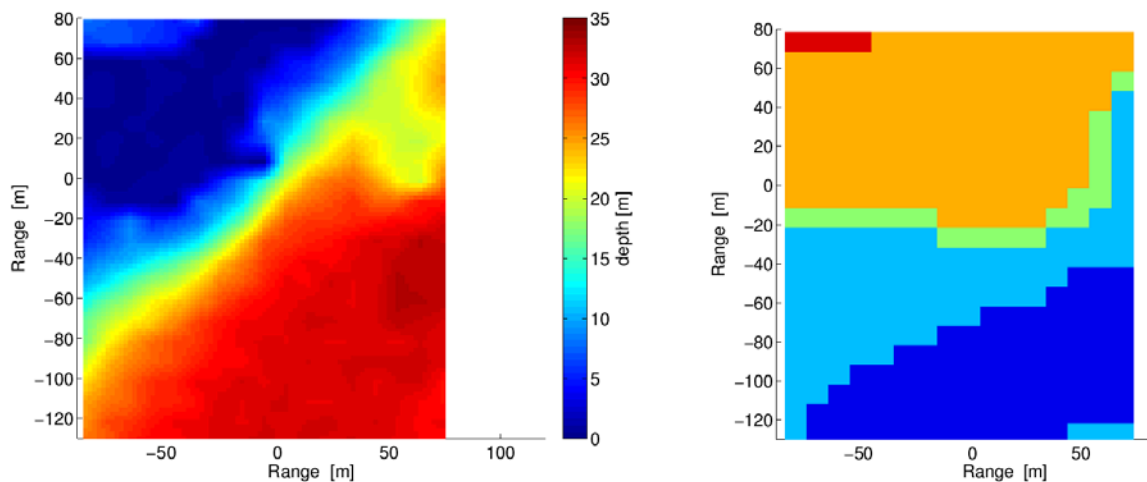

Fig. 1. Horizontal maps showing bathymetry (left) and bottom type (right). The receiver is at the origin in the indicated coordinate system (*xy*), and the source is about 50 m to the south, at $(x,y) =$ (−8m,−51.5m). The bottom types are postglacial clay (dark-blue), thicker glacial clay (light-blue), thinner glacial clay (green), crystalline rock (orange), and sand (red).

The impulse response recordings by a single hydrophone in the array show initial isolated peaks, followed by long decaying spiky tails. A 3-D ray model, Rev3D, was used to model the measured time traces. In Sec. 2, the initial peaks were identified as direct and multi-path propagation arrivals of various types. However, the propagation modelling was not able to explain the decaying tails. Reverberation modelling is thus included in Sec. 3. As in [4],[5],[6], it appears that the decaying tails arise from bistatic reverberation involving sea-bottom and sea-surface scattering from an elliptical horizontal area, with the source and receiver positions as focal points. Rev3D modelling with energy-density maps for selected time intervals and time traces for energy-weighted averages of various parameters were used to locate the parts of the bottom with the most significant contributions to the impulse response. In Sec. 4, beam-forming with the receiver array was also used for this purpose, and clear indications of 3-D horizontal refraction effects are noted. Some conclusions are stated in Sec. 5.

2. Propagation modelling of measured single-hydrophone data

Some details of the 3-D ray model Rev3D are given in [7],[5],[6]. Essential input data for propagation modelling are the sound-speed profile and reflection coefficients at the bottom as well as at the sea surface. Figure 2 shows this data for the present application. The bottom-reflection curves for the different bottom types show oscillations caused by an assumed layering in each case. With a wind speed of 8.5 m/s, the sea-surface reflection-coefficient curve in Fig. 2 indicates bubble-induced losses at low grazing angles [8].
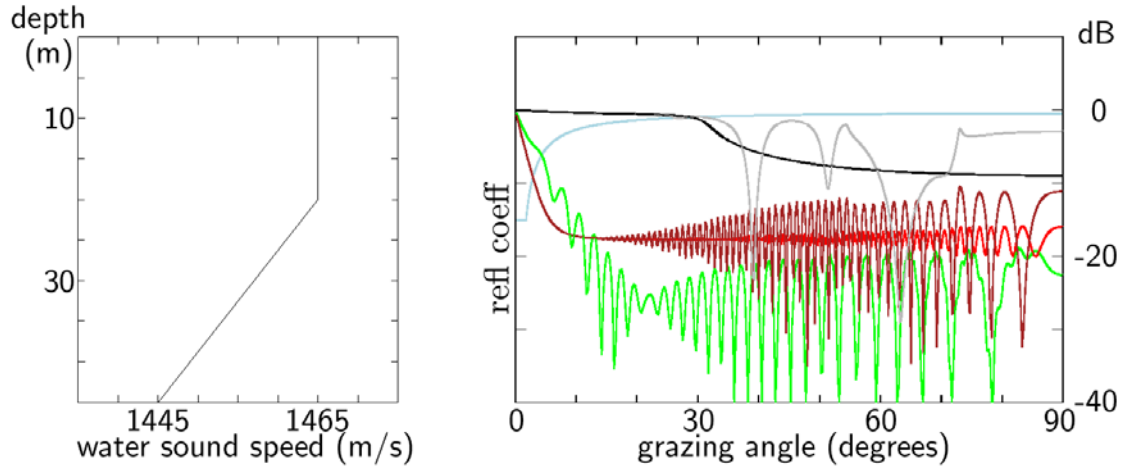
Fig. 2. Sound-speed profile (left), and reflection coefficients at 25 kHz, as functions of the grazing angle for the bottom and the sea surface (right). There are bottom reflection-coefficient functions for postglacial clay (green), thinner glacial clay (red), thicker glacial clay (brown), crystalline rock (grey), and sand (black). The blue curve shows reflection coefficients at the sea surface for a wind speed of 8.5 m/s, as measured in the experiment.

Figure 3 shows measured single-hydrophone time traces along with the corresponding Rev3D propagation modelling results. FM pulses with bandwidth 5 kHz were emitted, implying an effective pulse length of about 0.2 ms, with some precursor, after match-filtering. There are three panels in Fig. 3, one for each of the source depths 7.5 m, 15 m, and 22.5 m.

In each panel, the first arrival is a direct wave that has not been reflected at the bottom, or at the sea surface. Given noted level variations of several dB between different pings, the agreement between the measured, and modelled, direct arrivals is judged to be satisfactory.

The later propagation arrivals may be identified from Fig. 4; showing, as functions of traveltime t, average numbers of bottom reflections $N_b(t)$ and surface reflections $N_s(t)$ for the rays contributing to the modelled propagation time trace. For example, the second arrival is the initial surface reflection ($N_b=0$, $N_s=1$) when $z_s = 7.5$ m, and the initial bottom reflection ($N_b=1$, $N_s=0$) when $z_s = 22.5$ m.

Some details for computation of the time traces $N_b(t)$ and $N_s(t)$ are now described in a somewhat more general setting. Incoherent Rev3D propagation modelling, as used here, involves computation of the average intensity in a small box centered at the receiver. For a source intensity pulse $s(t)$, each ray u, with traveltime t_u, provides a contribution of strength T_u, and the modelled intensity time trace appears as $\varphi(t) = \sum_u T_u \, s(t-t_u)$. For an auxiliary quantity Q, for example N_b or N_s, with value Q_u for ray u, time traces

$$q_m(t) = \sum_u (Q_u)^m \, T_u \, s(t-t_u) \tag{1}$$

are defined for $m=0,1,2,\dots$ Apparently, $q_0(t) = \varphi(t)$, while $q_m(t)$ for $m > 0$ provide energy-weighted moments. In particular, $Q_a(t) = q_1(t)/q_0(t)$ gives energy-weighted averages of Q, with standard deviations $Q_s(t) = [\, q_2(t)/q_0(t) - Q_a^2(t) \,]^{\frac{1}{2}}$. Time traces for grazing angles and azimuthal angles, for example, are also of interest for arrival identification, cf. Sec. 4.
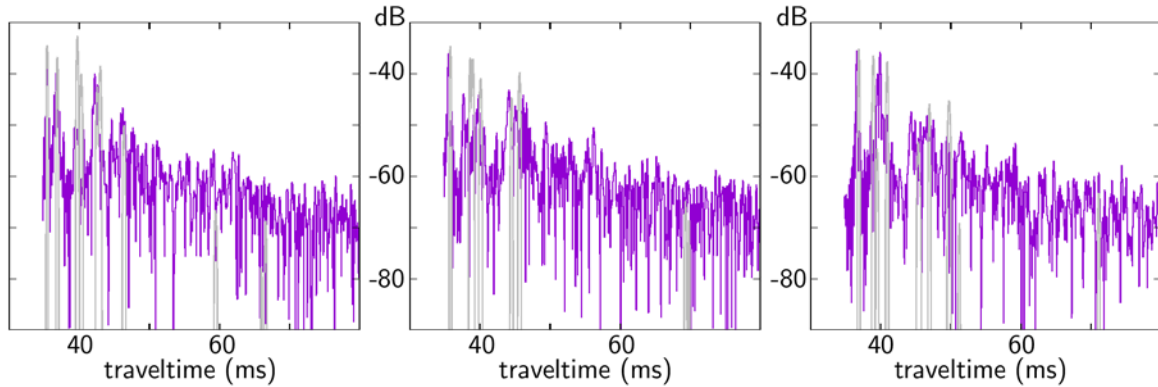
Fig. 3. Match-filtered measured time traces (violet) along with corresponding ones from Rev3D propagation modelling (grey). The source depths are 7.5 m (left), 15 m (middle), and 22.5 m (right). The dB values are given relative to the level at 1 m from the source.
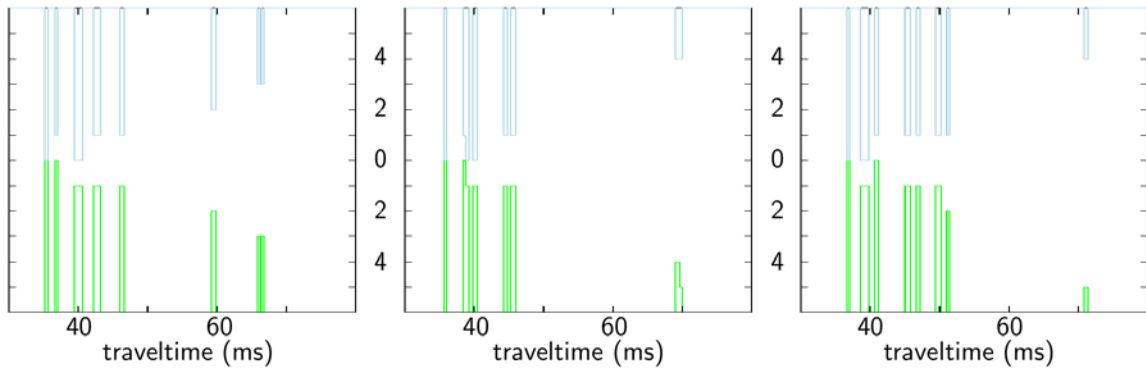

Fig. 4. Auxiliary time traces for the modelled propagation time traces in Fig. 3. The green and blue curves show average numbers of bottom and surface reflections, respectively. The source depths z_s are as in Fig. 3: 7.5 m (left), 15 m (middle), and 22.5 m (right).

Obviously, the propagation modelling only explains minor parts of the measured time traces in Fig. 2. Reverberation is included in Sec. 3 to model the rest.

3. Including bistatic reverberation in the modelling

Scattering kernels as in [6], giving the scattering strength for a unit area (1 m^2), are now introduced for the bottom and for the surface. They are functions of the grazing angles θ_1 and θ_2 for incoming and outgoing rays, respectively, and the bistatic angle β (the angle as viewed from the scattering point between the ray projections on the local scattering plane.). The chosen scattering kernels, denoted $S = S(\theta_1, \theta_2, \beta)$, are symmetric in θ_1 and θ_2.

For the bottom, a low-order small perturbation method (SPM) kernel S was selected, as specified by Eqs. (13.9), (13.21), (13.26), and (8.49) in [9], together with the "von Karman" roughness spectral density W according to Eqs. (D.7-8) there, with $\gamma_2 = 3$. The spectral density W includes the root-mean-square (rms) roughness height h and the roughness correlation length $l = 1/K_0$ as parameters. Figures 5-7 show some values for the relevant bottom types.
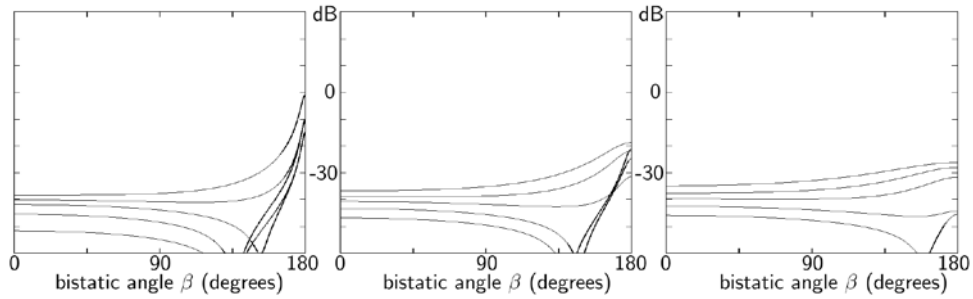
Fig. 5. SPM sea-bottom scattering strength $S(\theta_1,\theta_2,\beta)$ for postglacial clay as a function of the bistatic angle β at 25 kHz. The roughness height h, and correlation length l, are 2.5 and 25 cm, respectively. The three panels concern different values of the difference between the grazing angles of the incoming and outgoing rays: 0° (left), 15° (middle), and 30° (right). In each panel, the five curves show S values for different values of the least-grazing angle: from bottom to top 5°, 10°, 20°, 30°, and 40°.

A common feature for the kernels $S(\theta_1,\theta_2,\beta)$ in Figs. 5-7 are the increasing values when β approaches 180°, corresponding to forward scattering. The increase is particularly strong when $\theta_1 = \theta_2$, as shown in the left panels, when the specular scattering direction is approached. For fixed $|\theta_2-\theta_1|$, S increases with the grazing angles. There is a clear dependence on the bottom type, S is weakest for postglacial clay, and strongest for crystalline rock.
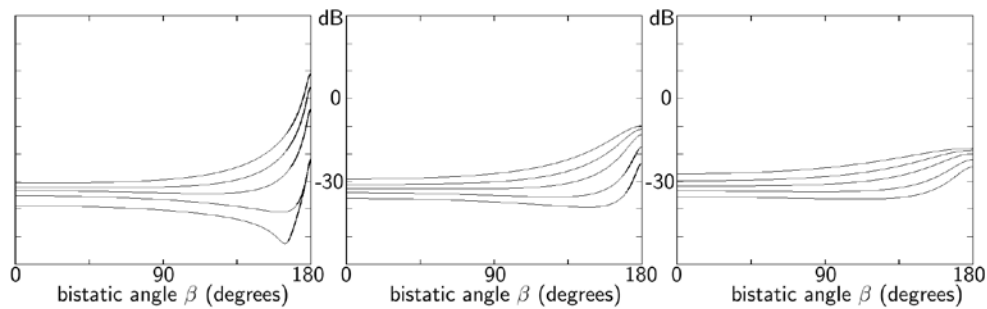

Fig. 6. As Fig. 5, but for glacial clay. The roughness parameters h and l are still 2.5 and 25 cm, respectively.

There are significant uncertainties in the assigned values for roughness height h (2.5 cm for postglacial and glacial clay, 2.0 cm for crystalline rock) and correlation length l (25 cm). References [9] and [10],[11] give some guidance, but the relation between h and grain size is only known in part [10], and there is no clear relation between l and sediment type [11].
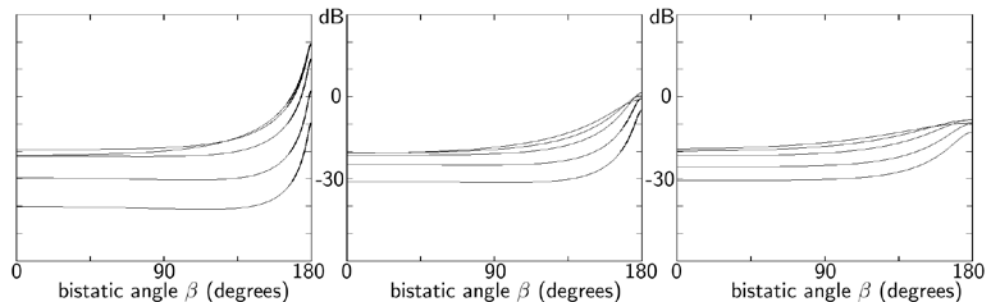

Fig. 7. As Figs. 5 and 6, but for crystalline rock. The roughness parameters h and l are now 2.0 and 25 cm, respectively.

For sea-surface scattering, the small-slope approximation (SSA) is applied in [4]. Here, however, a more easily implemented version of the composite roughness model was applied. As detailed in [6], contributions from bubble scattering and roughness/facet scattering were added. The roughness spectral density W, with the wind speed as a parameter, is now derived from the Pierson-Moskowitz gravity-wave frequency spectrum for a fully developed sea [8]. Figure 8 shows parts of the resulting kernel $S(\theta_1,\theta_2,\beta)$ with, as in Figs. 5-7, large forward scattering.
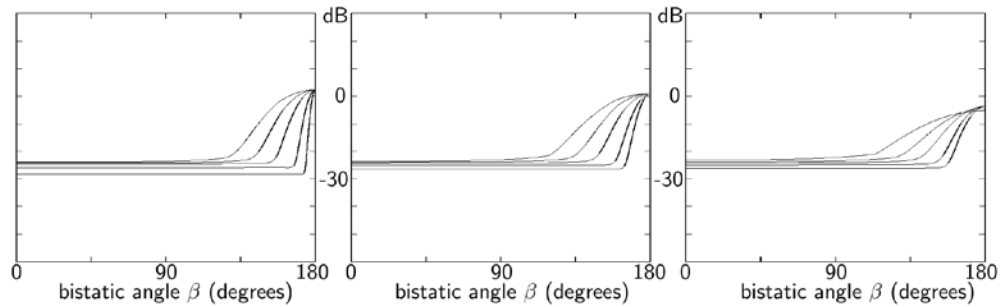

Fig. 8. Composite roughness sea-surface scattering strength $S(\theta_1,\theta_2,\beta)$ as a function of the bistatic angle β at 25 kHz. The wind speed is 8.5 m/s. In the same way as in Figs. 5-7, there are three panels, with five curves in each panel.

Figure 9 shows Rev3D reverberation time traces, computed with the specified scattering kernels, together with the measured data and the Rev3D propagation traces from Fig. 3. Inclusion of the bistatic reverberation in the modelling successfully explains the existence of long tails in the experimental data, and the decay rates are reasonably well matched. However, the spiky character of the measured reverberation is not matched. It is probably caused by clutter, recall the short effective pulse length of 0.2 ms enabling resolution of dm-size features, the modelling of which would require a very detailed knowledge of the bathymetry and the sea-surface roughness.
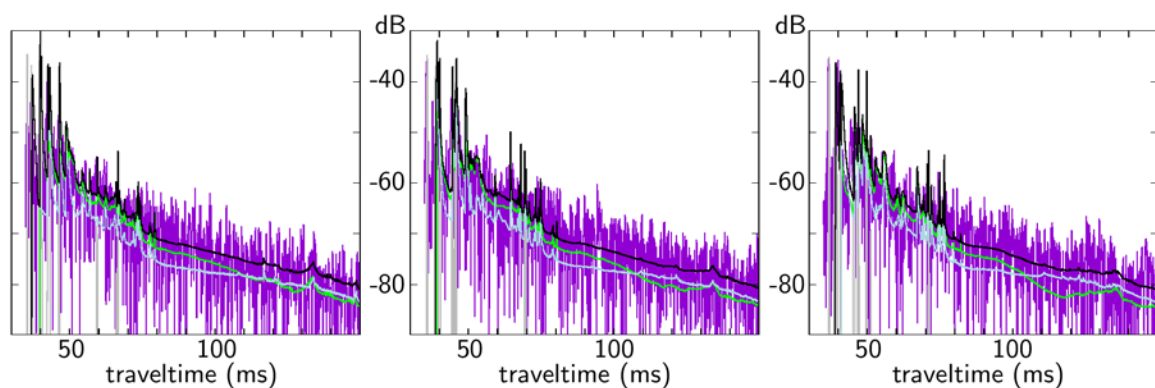

Fig. 9. Match-filtered measured time traces (violet) along with the corresponding ones from Rev3D propagation modelling (grey) and reverberation modelling (black). The modelled sea-bottom (green), and sea-surface (blue), reverberation traces are also shown separately. As in Fig. 3, the source depths are 7.5 m (left), 15 m (middle), and 22.5 m (right). The dB values are given relative to the level at 1 m from the source.

Figure 9 also shows the modelled sea-bottom, and sea-surface, reverberation traces separately. The bottom reverberation seems to dominate up to about 100 ms, after which the

contributions are of a similar size. As expected from the enhanced values of the scattering, kernels close to the specular direction (Figs. 5-8), propagation peaks in Fig. 9 give, in general, rise to reverberation peaks as well.

The Rev3D modelling includes information about the spatial scattering origin of the reverberation energy, for example, that can readily be extracted. Selecting the case with source depth 7.5 m, Figs. 10 and 11 show such information for sea-bottom and sea-surface reverberation, respectively. Early reverberation, between 35 and 80 ms (the left panels), is dominated by forward scattering, close to the specular direction, from cigar-shaped eccentric ellipses with the source and the receiver as focal points, cf. [12]. For the bottom reverberation, the bottom-type map from the right panel of Fig. 2, makes an imprint with significantly reduced contributions from the bottom parts with postglacial and glacial clay, cf. Figs. 5-7.

The late reverberation, between 85 and 120 ms in the right panels of Figs 10-11, arises from elliptical shells on the bottom and at the sea-surface. Particularly, for the bottom reverberation, the main contribution originates from the part of the shell with crystalline rock.
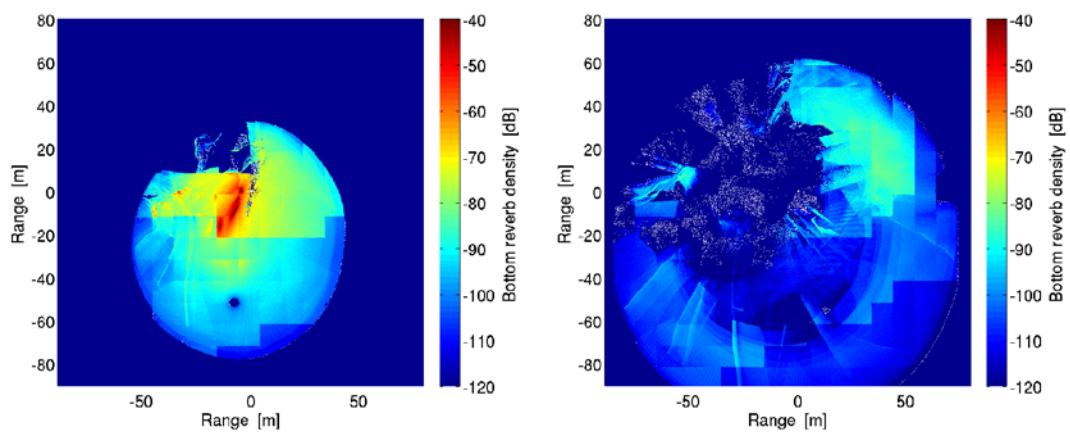

Fig. 10. Scattering origin in the horizontal plane of modelled sea-bottom reverberation, per unit horizontal surface area (1 m^2) and in dB. The source depth is 7.5 m. As in Fig. 1, the receiver is at the origin in the horizontal coordinate system, with the source about 50 m to the south. The left and right panels concern energy, with traveltime between 35-80 and 85-120 ms, respectively.
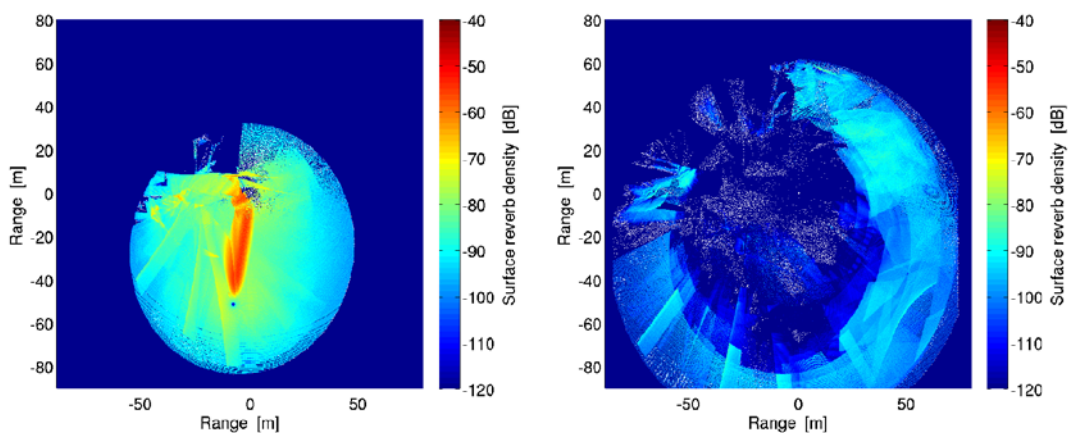

Fig. 11. As Fig. 10, but for modelled sea-surface reverberation.

In general, results such as those in Figs. 10-11 are helpful to improve the modelling and bring about a better match to the measured data. The modelled bottom reverberation at a

certain time segment, for example, is apparently modified if the bottom slopes or the bottom types are modified at the corresponding contributing parts of the bottom. With too-strong early reverberation, as indicated by Figs. 3 and 9, the assumed scattering strengths and reflection coefficients at parts of the region, between the source and the receiver, are probably somewhat too large.

   As a further aid in improving incoherent Rev3D reverberation modelling, as applied here, it is useful to study the time evolution of energy-weighted averages of certain auxiliary parameters. Basically, a Rev3D reverberation intensity time trace results, by summing contributions from patches or area elements, in a polar grid centred at the receiver. Rays are traced to the patches, at the sea-bottom and at the sea-surface, from the source (rays indexed u) as well as the receiver (rays indexed v), using reciprocity. For a source intensity pulse $s(t)$, the modelled intensity time trace appears as $\varphi(t) = \sum_{\text{patches}} dA \sum_u \sum_v T_u R_v S_{u,v} s(t-t_{T,u}-t_{R,v})$. Here, dA is the area of the pertinent patch, T_u and R_v are the average intensities over the patch contributed by rays u and v, respectively, $t_{T,u}$ and $t_{R,v}$ are the corresponding traveltimes, while $S_{u,v}$ is the scattering strength (per unit scattering area, 1 m^2) for the ray angles involved.

   For an auxiliary quantity Q, e.g., the bistatic angle β, with value $Q_{u,v}$ for the ray pair u,v, time traces

$$q_m(t) = \sum_{\text{patches}} dA \sum_u \sum_v (Q_{u,v})^m T_u R_v S_{u,v} s(t-t_{T,u}-t_{R,v}) \qquad (2)$$

are now defined for $m=0,1,2,…$ Apparently, $q_0(t) = \varphi(t)$, while $q_m(t)$ for $m > 0$ provide energy-weighted moments. Exactly as noted in connection with Eq. (1), $Q_a(t) = q_1(t)/q_0(t)$ gives energy-weighted averages of Q, with standard deviations $Q_s(t) = [\, q_2(t)/q_0(t) - Q_a^2(t) \,]^{1/2}$.
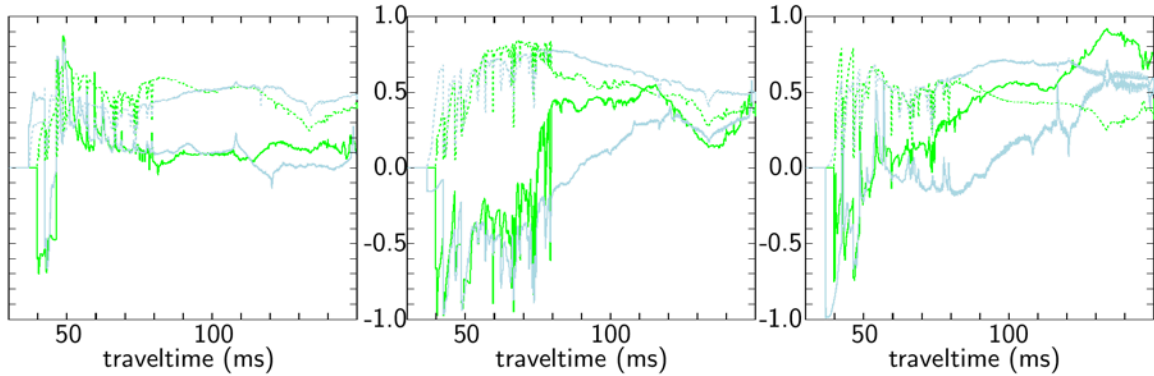

Fig. 12. Time evolution of sin φ_R (left), cos η_R (middle) and sin η_R (right). The green and blue curves concern bottom and surface reverberation, respectively. The solid curves show energy-weighted averages, and the dashed ones show the corresponding standard deviations. The source depth is 7.5 m.

   For the source depth 7.5 m, Fig. 12 shows energy-weighted time evolution traces of this kind for sin φ_R and cos η_R, sin η_R, where φ_R and η_R are the apparent direction angles to the sources of the incoming energy at the receiver. The vertical angle is denoted φ_R, positive upwards, and the horizontal (azimuthal) angle is denoted η_R, 0° to the east and 90° to the north. As expected, sin φ_R is mainly positive (negative) for the early surface (bottom) reverberation. The dips with large negative values of cos η_R at traveltimes between 35 and 80 ms correspond to strong forward scattering close to the specular direction, cf. Figs. 9-11. The mainly positive values of cos η_R as well as sin η_R for the bottom reverberation between 85 and 120 ms correspond to arrivals from the north-east, which is consistent with the right panel of

Fig. 10. Time traces for numbers of bottom and surface reflections could, of course, be studied not only for propagation, cf. Fig. 4, but for reverberation as well.

4. Modelling of beam-formed array data

The experimental time traces in Figs. 3 and 9 were obtained by a single hydrophone. Beam-forming with the linear receiver array, 1 m long with 32 hydrophones, was then applied to verify some of the Rev3D results from Figs. 10-12.

Two array configurations were used during the experiment: horizontal deployment perpendicular to the direction to the source, and vertical deployment. At 25 kHz as the center frequency of the FM pulse, a lobe width of a few degrees, and a side-lobe suppression of some 30 dB is expected for the broad-side beam (using weighted beam-forming with correction for wave-front curvature). However, the observed side-lobe suppression does not exceed 15-20 dB. A slight misalignment of the hydrophones in the array could be one explanation, but there are other possibilities.

Figure 13 shows beam-forming results for the horizontal array deployment compared to modelling, for the source depth 7.5 m. The modelling results, in the right panel, are obtained without beam-forming by positioning the ray-arrival energy at bins in the traveltime-η plane. Here, η (eta) is the azimuth, zero for an arrival from the source and positive (negative) for an arrival from the east (west), cf. Fig. 1. For each bin, it is the summed energy that is shown, including propagation as well as reverberation contributions. Each bin has size 0.2 ms concerning traveltime, and one degree concerning angle. The initial arrival is, of course, the direct wave, and it is followed by the primary surface reflection. Figure 4 is useful for the arrival identification. Interestingly, the subsequent bottom reflections exhibit significant azimuth shifts caused by horizontal refraction. As expected, the propagation arrivals involving bottom or surface reflection are accompanied by significant reverberation energy at near-by bins in the t-η plane.
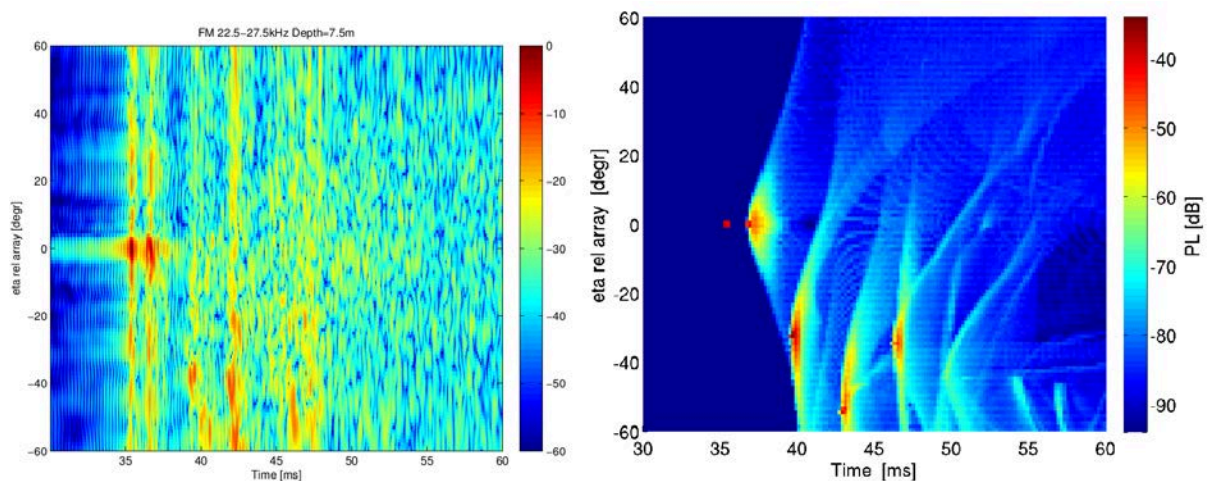

Fig. 13. Received energy positioned in the traveltime-azimuth (t-η) plane, with $\eta = 0^{\circ}$ for the source direction, and a negative value for energy from the west. The left panel shows experimental results obtained by beam-forming, in dB relative to the maximum. The right panel shows modelling results, obtained by binning the received energy without beam-forming, in dB relative to the level at 1 m from the source, implying about −34 db for the direct wave. In each panel, the dB scale covers 60 dB. The source depth is 7.5 m.

The deficient side-lobe suppression at the beam-forming implies considerable smearing in the η direction of the arrivals in the left panel of Fig. 13. Nevertheless, the direct wave and the primary surface reflection, are clearly seen. It is also tempting to identify the red spots between about 39 and 46 ms as the bottom arrivals noted in the right panel, and in the left panel of Fig. 4, and take the azimuth shifts of about 30 to 55 degrees as experimental evidence of horizontal refraction.

Exact agreement of travel time and azimuth shifts for the bottom-interacting arrivals in the two panels of Fig. 13 is of course not expected, since the bottom topography is not known exactly. Travel time errors of a few ms are not unreasonable, and reflection angles are obviously sensitive to the local bottom slope.

At large $|\eta|$, when the end-fire direction is approached, the beam-forming with the horizontally deployed array actually implies some vertical directivity. The effect is not very important in Fig. 13, however, with its restriction to $|\eta| < 60^{\circ}$. Figure 14, for the vertical array deployment, focuses on the vertical directivity. The arrival energy is now plotted in the t-φ plane, where φ is the inclination angle, positive for energy arriving from above. In the right panel, the modelled direct wave appears at $\varphi \approx 0^{\circ}$, which is consistent with the coinciding source and receiver depths, 7.5 m. However, there is a misalignment of a few degrees in the experimental result, probably caused by inaccurate depth measurements. The primary surface and bottom arrivals appear with positive and negative φ, respectively.
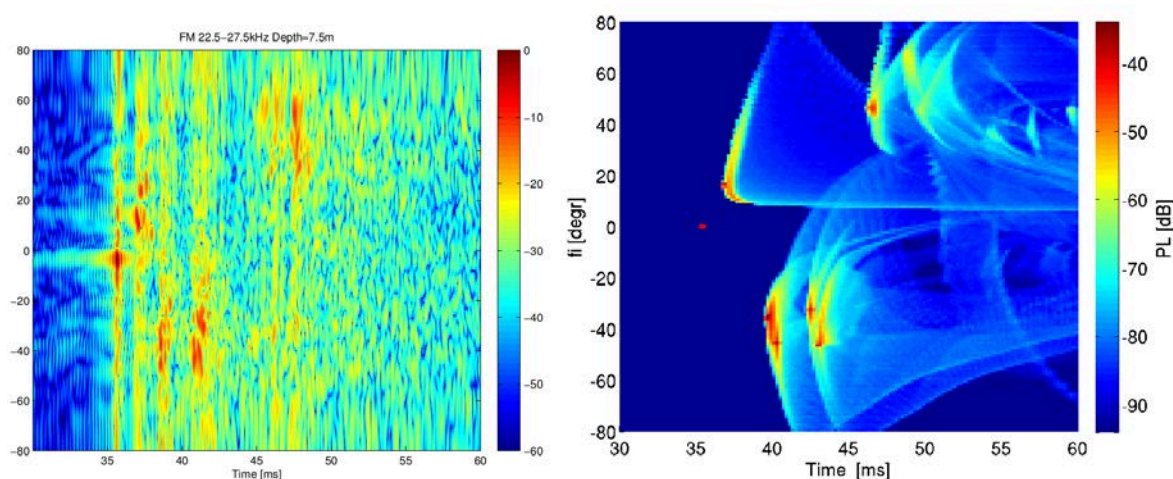

Fig. 14. Received energy positioned in the traveltime-inclination (t-φ) plane, with φ positive for energy from above. As in Fig. 13, the left and right panels show experimental and modelling results, respectively. The source depth is still 7.5 m.

5. Conclusions

The high-frequency (25 kHz) impulse response in a short-range experiment in shallow water showed a long decaying spiky tail, which is difficult, if not impossible, to explain by ordinary 2-D propagation modelling. Using Rev3D, a 3-D ray model, it appears that the spiky tail is caused by bistatic out-of-plane scattering and reverberation, from the bottom as well as the sea surface. Thus, the present study gives further support to the idea that such scattering must be included in model-based simulators of underwater communication and sonar performance, where high-fidelity modelling of the impulse response is required.

Auxiliary time traces, and energy-density maps of various kinds, can help to identify the different contributions to a modelled impulse response. Energy-weighted time traces are used in the propagation modelling in Sec. 2 for average numbers of bottom and surface reflections, in the reverberation modelling in Sec. 3 for average arrival directions at the receiver, and in Section 4 to study the combined propagation and reverberation energy in traveltime-angle planes. Section 3 also shows maps for the origin at the bottom, and at the sea surface, of reverberation energy received during specified time intervals. Beam-forming with an array, deployed horizontally as well as vertically, is used in Sec. 4 for experimental verification. Clear azimuthal shifts for certain arrivals indicate 3-D effects of a horizontal-refraction type.

The early modelled reverberation in Fig. 9 is somewhat too strong. The assumed scattering strengths and reflection coefficients at parts of the region between the source and the receiver may be too large. Furthermore, it is known that the accuracy of the applied bottom-scattering kernel of SPM type deteriorates close to the specular direction. Implementation of SSA alternatives [9] are desirable, as is inclusion of sediment volume scattering, e.g., [13], [14]. For further experimental studies of the impulse response, very accurate knowledge of the bottom topography and array measurements with good side-lobe control would be valuable.

Acknowledgement

References

[1]   P.H. Dahl, 'High-frequency forward scattering from the sea surface: The characteristic scales of time and angle spreading', IEEE J. Ocean. Eng. 26, 141-151, 2001.

[2]   D.G. Simons, R. McHugh, M. Snellen, N.H. McCormick, and E.A. Lawson, 'Analysis of shallow-water experimental acoustic data including a comparison with a broad-band normal-mode-propagation model', IEEE J. Ocean. Eng. 26, 308-323, 2001.

[3]   P.A. van Walree, 'Propagation and scattering effects in underwater acoustic communication channels', IEEE J. Ocean. Eng. 38, 614-631, 2013.

[4]   J.W. Choi and P.H. Dahl, 'Measurement and simulation of the channel intensity impulse response for a site in the East China Sea', J. Acoust. Soc. Am. 119, 2677-2685, 2006.

[5]   T. Jenserud and S. Ivansson, 'Measurements and modeling of effects of out-of-plane reverberation on the power delay profile for underwater acoustic channels', IEEE J. Ocean. Eng. 40, 807-821, 2015.

[6]   S. Ivansson and T. Jenserud, 'Assessing effects of sea-bed and sea-surface scattering on acoustic propagation', Proc. Inst. Acoust. 37, 807-821, 2015.

[7]   S. Ivansson, 'Stochastic ray-trace computations of transmission loss and reverberation in 3-D range-dependent environments', Proc. 8th ECUA, 131-136, 2006.

[8]   M.A. Ainslie, 'Principles of Sonar Performance Modeling', Springer, 2010.

[9]   D.R. Jackson and M.D. Richardson, 'High-Frequency Seafloor Acoustics', Springer, 2007.

[10] K.B. Briggs, 'Microtopographical roughness of shallow-water continental shelves', IEEE J. Ocean. Eng. 14, 360-367, 1989.

[11] K.B. Briggs, A.P. Lyons, E. Pouliquen, L.A. Mayer, and M.D. Richardson, 'Seafloor roughness, sediment grain size, and temporal stability', Proc. 1st UAM, 337-343, 2005.

[12] C.H. Harrison, 'Closed form bistatic reverberation and target echoes with variable bathymetry and sound speed', IEEE J. Ocean. Eng. 30, 660-675, 2005.

[13] D.R. Jackson, R.I. Odom, M.L. Boyd, and A.N. Ivakin, 'A geoacoustic bottom interaction model (GABIM)', IEEE J. Ocean. Eng. 35, 603-617, 2010. (Correction in IEEE J. Ocean. Eng. 36, 373, 2011.)

[14] P.L. Nielsen, R.D. Hollett, G. Canepa, and W.L.J. Fox 'Unique low-frequency mine hunting and seabed characterization sonar', Proc. 1st UA, 385-392, 2013.